Crystallization of the Large Membrane Protein Complex Photosystem I in a Microfluidic Channel

Bahige G. Abdallah, Christopher Kupitz, Petra Fromme, and Alexandra Ros*

Department of Chemistry and Biochemistry, Arizona State University, Tempe, Arizona 85287, United States

ABSTRACT Traditional macroscale protein crystallization is accomplished non-trivially by exploring a range of protein concentrations and buffers in solution until a suitable combination is attained. This methodology is time-consuming and resource-intensive, hindering protein structure determination. Even more difficulties arise when crystallizing large membrane protein complexes such as photosystem I (PSI) due to their large unit cells dominated by solvent and complex characteristics that call for even stricter buffer requirements. Structure determination techniques tailored for these "difficult to crystallize" proteins such as femtosecond nanocrystallography are being developed yet still need specific crystal characteristics. Here, we demonstrate a simple and robust method to screen protein crystallization conditions at low ionic strength in a microfluidic device. This is realized in one microfluidic experiment using low sample amounts, unlike traditional methods where each solution condition is set up separately. Second harmonic generation microscopy *via* second-order nonlinear imaging of chiral crystals (SONICC) was applied for the detection of nanometer- and micrometer-sized PSI crystals within microchannels. To develop a crystallization phase diagram, crystals imaged with SONICC at specific channel locations were correlated to protein and salt concentrations determined by numerical simulations of the time-dependent diffusion process along the channel. Our method demonstrated that a portion of the PSI crystallization phase diagram could be reconstructed in excellent agreement with crystallization conditions determined by traditional methods. We postulate that this approach could be utilized to efficiently study and optimize crystallization conditions for a wide range of proteins that are poorly understood to date.

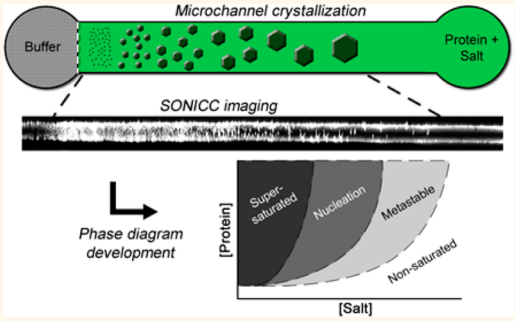

KEYWORDS: membrane protein · concentration gradients · numerical simulation · SONICC

Protein crystallization can be a daunting task and often takes years to optimize for a given protein. Typically, a screening process is employed in which many conditions of various protein concentrations and buffers are tested separately until an optimal combination initiates crystallization.[1−4] Crystallization is a necessary precursor of crystallography, which is the most commonly used method to elucidate protein structure, requiring highly ordered protein crystals in order to obtain high-resolution X-ray diffraction patterns to analyze the atomic arrangement of a protein.[5] Usually, the chosen X-ray beam technology governs the types and quality of crystals desired leading to further crystallization screening and optimization for a specific crystal characteristic. In traditional crystallography, the high dose of X-ray radiation requires large crystals to avoid damage before diffraction and to provide suitable electron density.[6]

Many complex proteins such as membrane proteins pose even greater difficulties during crystallization method development and in many cases are nearly impossible to crystallize at sizes suitable for traditional crystallography, which is why less than 400 out of the 80 000+ protein structures determined to date comprise membrane proteins.[7] The main reason for this is that membrane proteins have large unit cells dominated by solvent (>70%) where solvent−protein interactions dominate, leaving few contact areas for protein−protein interactions. Consequently, increased disorder arises in the unit cell arrangement, eventually preventing ordered crystal formation.[8] For example, it took 12 years to determine the structure of photosystem I (PSI) at atomic resolution with the majority of this

* Address correspondence to alexandra.ros@asu.edu.

Received for review May 18, 2013 and accepted November 5, 2013.

Published online November 05, 2013
10.1021/nn402515q

time being spent developing a crystallization method to provide suitable crystals.[7] This was a significant accomplishment as PSI is the largest and most complex membrane protein crystallized to date consisting of 36 proteins to which 381 cofactors (chlorophylls, carotenoids, quinones, and 4Fe4S clusters) are noncovalently attached.[7] One can imagine that the ability to easily grow membrane protein crystals would drastically expedite structure determination. However, an alternative route is the current development of femtosecond nanocrystallography which is tailored for complex membrane protein structure determination where smaller, ideally nanometer-sized crystals can be utilized to provide diffraction patterns.[9,10] Yet femtosecond nanocrystallography still imposes some desired crystal characteristics such as a monodispersed suspension of nanocrystals, thus it is imperative to optimize crystallization conditions to obtain such samples as well as to develop methods to characterize sample size distributions.[11]

Microfluidic devices have become widespread in their application toward biochemistry[12] including areas such as electrophoresis,[13−15] PCR,[16−18] immunoassays,[19−21] biosensors,[22−24] and more.[25−28] Protein crystallization has also been demonstrated in capillaries[29−31] and a microfluidic device[32] by means of counter-diffusion[33] in which lysozyme and insulin, among others, have been crystallized. In these experiments, protein and crystallization buffer concentration gradients form along a channel in which many conditions can be realized in one experiment. Controlled mixing of two reagents by microfluidic droplet generation[34] has also been employed for crystallization screening[35] in which protein and buffer are interspersed within a droplet. These methods have been applied to the more common high ionic strength "salting-in" procedures for proteins with well-known crystallization characteristics where a separate saline buffer or buffer containing precipitants like polyethylene glycol come into contact with protein solution. Low ionic strength crystallization which lacks any precipitant, such as that employed for the membrane protein complex PSI,[8] has not yet been demonstrated in a microfluidic device to the best of our knowledge.

The reason behind this alternate crystallization pathway for PSI is due to the many factors influencing the solubility of proteins including ionic strength, pH, and precipitant concentration, among others. In typical salting-in crystallization procedures, protein solubility is generally highest at medium ionic strength and decreases at high ionic strength due to competition between ions and protein for the solvent water. However, solubility is also decreased at very low ionic strength as charged groups on the protein surface are depleted of counterions, thereby facilitating crystal contact formation between oppositely charged groups on nearby protein molecules. This latter effect is referred to as the "reverse of salting-in" and occurs with PSI.[36] Specifically, the salt ($MgSO_4$) and the protein coexist in one solution, and microfluidic crystallization is accomplished by diffusion of the salt ions (Mg^{2+} and SO_4^{2-}) at a faster rate than the protein. This is possible due to the large difference in diffusion coefficients between the salt ions and protein, resulting in a temporal ionic strength gradient within the protein solution capable of probing various conditions in a crystallization phase diagram within one experiment.

Establishing a salt gradient within the microchannel requires the presence of a large reservoir to accept the diffusing salt ions, thus reducing the salt concentration of the protein solution. A crystallization buffer free of $MgSO_4$ is brought into contact with the salt-containing protein solution at a defined interface in a similar fashion as the introduction of a high ionic strength buffer in the opposite salting-in crystallization regime. In either case, direct mixing of the two solutions would cause rapid changes in protein and salt concentration that are beyond the kinetics of crystallization causing the protein to "crash out" of solution and form an amorphous precipitate.[37] Defined initial conditions, a stable interface, and convection-free conditions are thus important for microchannel crystallization experiments to establish optimized and reproducible crystallization conditions. Furthermore, quantitatively modeling concentration changes of participating ions becomes difficult when convection occurs as it can be caused by a variety of factors such as density gradients and evaporation.

Most capillary crystallization experiments employing diffusion-based crystallization methods implement gels to reduce convection[32,38−40] usually by adding a low concentration of gel to the protein solution to increase viscosity. However, this alters the crystallization conditions in a way that could pose problems when translated to macroscale crystallization experiments when large amounts of crystals are needed. To avoid this, the gel acupuncture method (GAME)[41,42] has been developed for capillary counter-diffusion crystallization. In this method, the capillary is filled with protein solution and partially punctured into a gel base saturated with crystallization buffer, thus establishing a porous barrier between the crystallization buffer and protein solution to effectively reduce convective mass transport. Here, we have adapted this method to a microfluidic channel in which the protein solution in the channel forms an interface with a gel-filled reservoir at the opposing channel end where salt-free buffer is added. Over time, salt ions diffuse out of the microchannel, forming an ionic strength gradient to induce crystallization at points along the channel where optimal conditions are met.

In this work, we demonstrate the ability to crystallize the membrane protein complex PSI using a gel barrier

and diffusion of salt and protein within a microfluidic device. Furthermore, we have incorporated a hydrophobic valve to set up a discrete crystallization zone, making quantitative analysis possible. Crystal formation along a microchannel was investigated with both bright-field microscopy as well as an effect known as second harmonic generation using second-order nonlinear imaging of chiral crystals (SONICC). To the best of our knowledge, SONICC was applied for the first time to the imaging of a protein crystallization process within a microfluidic channel, where we exhibit the capability of this technology to detect PSI crystals in the micrometer- and nanometer-size domains. Lastly, by correlating numerical simulations of the protein and salt concentrations along the channel to crystals imaged with SONICC, we illustrate the potential for efficient crystallization phase diagram development by producing a portion of the PSI phase diagram.

THEORY

An important aspect of this method is quantitative analysis to determine the actual concentrations of protein and salt that induce spontaneous nucleation (initial formation of stable protein clusters) and crystallization as well as a successful piecing together of the crystallization phase diagram of a protein. In our channel layout, two reservoirs are present at both channel ends (see Figure 1a). Initially, protein solution flows into the channel *via* capillary action. For quantitative analysis, a discrete, consistent crystallization zone is necessary, which is provided by the linear channel. Furthermore, leakage of protein solution into the opposing reservoir would cause variable concentrations of protein and salt in that reservoir that cannot be quantified. To overcome this, a hydrophobic valve was developed at the channel/gelled reservoir interface. At the valve, capillary action is halted since it is driven by surface tension (γ) along the hydrophilic channel.[43,44] The Young−Laplace equation[45] describes the relationship between surface tension, capillary pressure (p_c), and surface contact angle (θ):

$$p_c = \frac{2\gamma \cos\theta}{r} \quad (1)$$

where r is the radius of the fluid meniscus. At hydrophobic contact angles (>90°), p_c becomes negative; thus placing the valve at the channel end effectively halts capillary flow of the protein at the interface of the gelled reservoir to establish a discrete crystallization region within the channel.

The concentrations of salt and protein within the microfluidic channel are determined by numerical modeling using the representative geometry and considering the diffusion coefficients (D) of the salt ions[46] (Mg^{2+}: 7×10^{-10} m^2/s, SO_4^{2-}: 1×10^{-9} m^2/s) and protein (in channel: 2×10^{-11} m^2/s, in gel:[47] 9×10^{-12} m^2/s). A smaller PSI diffusion coefficient was considered in the gelled reservoir due to the large size of PSI and was calculated based on a theoretical model given by Boyer and Hsu that accounts for protein mass and agarose concentration.[47] The diffusion coefficients of the salt ions were assumed to have a negligible change in agarose gel. The numerical simulations are based on Fick's second law for time-dependent diffusion:[48]

$$\frac{\partial c}{\partial t} = D\nabla^2 c \quad (2)$$

where c is concentration, t is time, and ∇ is the gradient operator. The discrete crystallization region along the channel was modeled, and concentration profiles were obtained spanning the entire channel length for various experimental durations. When the actual experiment was imaged, various locations along the channel where crystals were observed were correlated to the simulations that correspond to the duration of the experiment at hand. Our aim was to use this quantitative information to form a phase diagram for PSI which compares protein concentration to salt concentration and assigns these concentrations to the various crystallization phases: *nonsaturated* where salt concentration is too high and crystallization does not occur, *metastable* where crystallization can occur nonspontaneously, *nucleation* where crystallization is spontaneous, and *supersaturated* where salt concentration is so low that protein precipitates rapidly and forms amorphous precipitate.[49]

RESULTS AND DISCUSSION

The working principle of the microfluidic crystallization device is first discussed. Figure 1a shows a longitudinal cross section of the channel and two reservoirs where PSI and buffer A (see Methods) were added. The channel was rendered hydrophilic by oxygen plasma treatment which facilitated filling of the channel with aqueous protein solution *via* capillary action. Because the opposing reservoir was punched postplasma treatment, the reservoir walls remained hydrophobic. Our fabrication technique is beneficial compared to chemical surface treatments, avoiding an added fabrication step and possible adverse reactions with the sample. As the protein fills the channel *via* capillary pressure, it eventually meets hydrophobic regions in the reservoir which halt the flow, acting as a hydrophobic valve.[50] Figure 1b illustrates a channel/reservoir interface without this valve where protein leaks into the reservoir as opposed to Figure 1c, which shows the valve effectively impeding protein flow. This barrier was necessary in order to eliminate leakage of the protein solution into the opposing reservoir where mixing could occur with buffer A/agarose during initial filling of the device. Furthermore, initial experiments demonstrated that the pipetting steps for filling both reservoirs could not be performed in a synchronized manner to ensure defined initial conditions for the

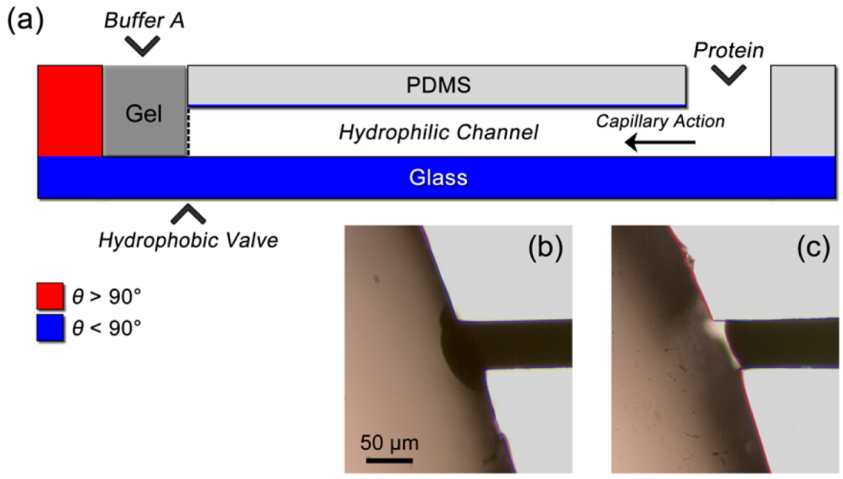

Figure 1. (a) Cross section of the microfluidic channel used for crystallization. Two reservoirs are located at channel ends where solutions can be introduced. The saline protein solution is injected into the channel from the reservoir on the right and fills *via* capillary action. The hydrophobic valve is placed at the left channel end to stop protein flow, effectively setting up a discrete crystallization zone. Hydrophobic surfaces are indicated in red, and blue designates hydrophilic regions. On the left side of the image, the reservoir containing the buffer A gel plug is shown. (b) Photograph of the buffer A reservoir/channel interface without the hydrophobic valve illustrating leakage of protein out of the channel and into the reservoir. (c) Photograph of the same interface with the hydrophobic valve showing impeded protein flow and no leakage out of the channel.

microfluidic crystallization experiment, fortifying the need for a valve barrier. Once the channel was filled, the empty second reservoir was filled with molten agarose that was gelled and saturated with buffer A to aid in the depletion of salt in the channel. Without a gel barrier, convective mixing was observed in which buffer A flowed rapidly into the channel and depleted the protein solution without crystallization (not shown). To reduce this effect, it is common practice to gel the protein solution during diffusion-based microfluidic crystallization;[32,38−40] however, our method eliminates the need to alter the protein solution (which can influence crystallization) by using a stand-alone gel plug.

Figure 2 shows a top-down perspective of the channel with drawn hexagonal PSI crystals of various sizes and abundance at their expected locations along the channel. Due to diffusion, ionic strength and protein concentration gradients form. As shown by the triangular scale, these two gradients decrease toward the gelled, initially protein-free reservoir, as indicated by the black to white color gradient. At the lowest ionic strength (white region of the scale), proteins precipitate out of solution rapidly and form amorphous precipitate instead of crystals. In the direction toward the protein reservoir (black region of the scale), crystal size increases and abundance decreases as crystallization kinetics change based on the salt and protein concentrations. At higher salt concentrations, the loss of interaction between the PSI trimers and salt ions is less extensive, thus a single crystal can build upon itself as less new nucleation events occur. The opposite occurs at lower salt concentrations because more free PSI trimer is present, thus the chance for new nucleation events is greater.

Numerical Simulations. In order to determine the concentrations of salt and protein along the channel, numerical simulations were employed. The model considered diffusion of both salt ions (Mg^{2+} and SO_4^{2-}) and PSI spanning the entire channel geometry which was replicated identically to that used experimentally. Diffusion was based on Fick's laws, and diffusion coefficients of the salt ions and proteins were considered as described in the Theory section. Because diffusion out of the channel occurred into the gelled reservoir, the diffusion coefficient of PSI in agarose was calculated based on a relationship between its estimated diffusion coefficient in water and the concentration of the agarose that it diffuses into, as developed by Boyer and Hsu.[47] It was assumed that diffusion of the salt ions was not influenced by the gel; therefore, their diffusion coefficients remained the same in the gel.

The simulations were solved as a time-dependent study, and four time durations were studied: 3, 6, 10, and 14 days. Concentration profiles of both salt ions (Figure 3a,b) and protein solution (Figure 3c) were developed. At 3 days, the concentration profiles of both salt ions show a slightly curved trend with the lowest concentration near the gelled reservoir (0 cm) and increasing concentration as the protein reservoir (3 cm) is approached, as shown in Figure 3a,b. As time increases to 6 days and greater, the salt ions develop a linear concentration profile with a decreasing slope. At very long durations, >4 months (not shown), the concentration profile becomes completely horizontal, indicating a homogeneous, equilibrated concentration distribution spanning the entire microchannel with a concentration of half the initial value. The profiles of both ions are comparable due to the similarity of their

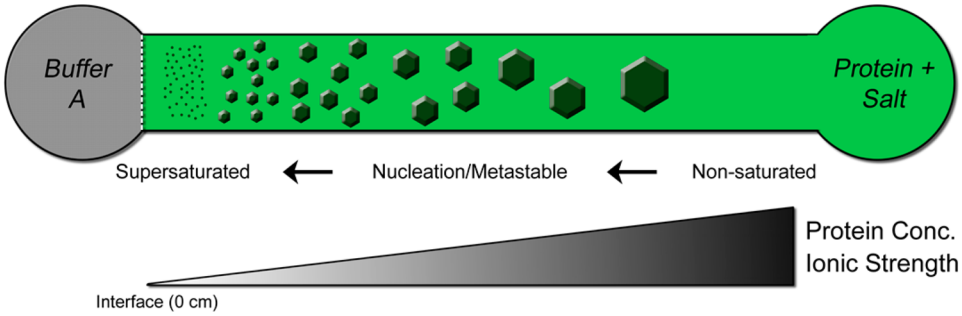

Figure 2. Top-down view of the channel structure, laid out similarly to that in Figure 1. PSI crystal characteristics are drawn within the channel as hexagons, indicating expected changes along the channel. At the gel/channel interface, salt concentration is the lowest; therefore, protein rapidly precipitates out of solution and forms amorphous precipitate (small dots). Moving toward the protein solution reservoir, crystal size increases and abundance decreases. In terms of the phase diagram, each phase can be mapped out along the channel beginning with supersaturated near the gel/channel interface and transitioning toward nonsaturated at the opposite end of the channel.

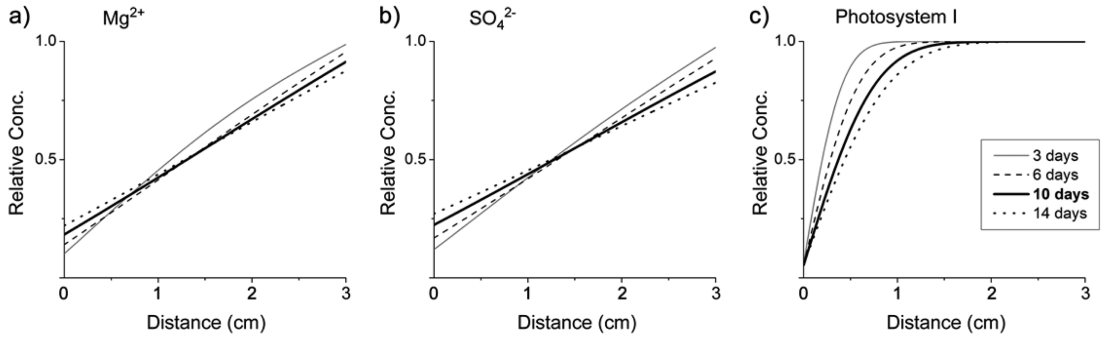

Figure 3. Simulated relative concentration profiles of protein and both salt ions along the microfluidic channel. Distance on the *x*-axis is the location relative to the gel/channel interface (0 cm). The simulations consider spatial and time-dependent diffusion of Mg^{2+} (a), SO_4^{2-} (b), and PSI (c). Each plot shows the concentration profiles at four different time points ranging from 3 to 14 days. At 3 days, the ions exhibit a slightly curved trend that becomes linear at later time points. The PSI curves show a hyperbolic trend due to its lower diffusion coefficient compared to the ions. The 10 day profile given by the solid bold line corresponds to the experimental data shown in Figure 4.

diffusion coefficients; however, the protein concentration profile differs significantly due to its diffusion coefficient being 1−2 orders of magnitude lower. Figure 3c shows the PSI concentration profile that maintains a hyperbolic type trend over all time durations plotted. At a much longer time compared to the salt ions (>10 years), the protein concentration profile does equilibrate in a similar fashion; however, this time duration is beyond the scope of any crystallization experiment that would be utilized for applications such as femtosecond nanocrystallography. It is important that the protein diffuses slowly, and its concentration remains high along a greater portion of the channel compared to that of the salt ions so that enough protein is available to crystallize. If both solutions were depleted, no crystals would form because there is simply not enough starting material. An ideal scenario would involve salt depletion along the channel in a linear gradient with minimal protein depletion to minimize interactions between the salt ions and PSI trimers, resulting in self-stabilization of the trimers by forming crystals.

Photosystem I Crystallization. Crystallization of PSI within a microfluidic channel was performed successfully using the reverse of salting-in diffusion method. After 3, 6, and 10 days of incubation, the channels were imaged using second harmonic generation *via* SONICC. This technology is based on the excitation of two photons which combine and emit as a single high-energy photon, a phenomenon that only occurs in noncentrosymmetric (lacking an internal plane of symmetry) species such as various protein crystals.[51,52] Individual protein molecules, amorphous precipitate, and the majority of salt crystals (including $MgSO_4$) do not possess this capability, thus this imaging technique can exclusively obtain a high contrast signal from protein crystals in complex mixtures or suspensions. A powerful imaging technique such as SONICC is crucial for our microfluidic crystallization experiments as the crystals in the channel were not isolated for further examination and were imaged directly on-chip. We were thus able to use SONICC to confirm the presence of crystals in the channel (and therefore a successful crystallization process) despite the dark green protein solution masking them under bright-field optical microscopy. Furthermore, SONICC provides the ability to detect small nanocrystals (<500 nm) that would be unresolvable with bright-field microscopy.

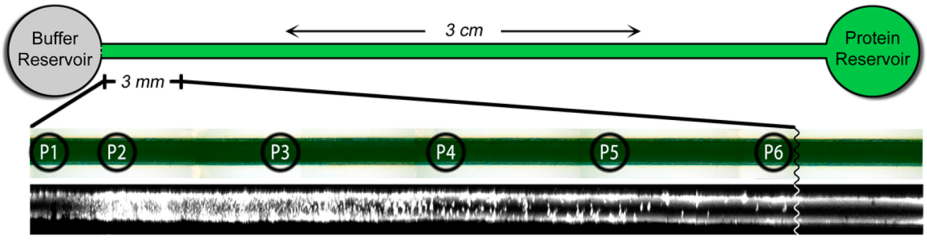

Figure 4. Microfluidic device dimensions with a zoomed in region showing SONICC and bright-field images of the microchannel: The capability of SONICC for detection is illustrated as a high contrast image compared to the bright-field image where crystals are not detectable in the dark protein solution. Only a small portion of the channel (3 mm) is shown where crystals were detected as further downstream conditions did not favor crystallization. Six positions are marked (P1–P6) corresponding to the labels shown on the phase diagram in Figure 5. The region depicted beyond P6 is representative of the remainder of the microchannel, which did not exhibit PSI crystals within the channel.

This is a major advantage for femtosecond nanocrystallography applications since we can determine crystallization conditions where nanocrystals are formed using our microfluidic platform in tandem with SONICC imaging. Figure 4 illustrates this ability, as the top sequence shows a bright-field image of the channel and the bottom sequence shows the corresponding SONICC image of a 10 day crystallization experiment. While the bright-field frames do not show crystals, the SONICC frames represent high contrast images clearly showing a strong signal from the PSI crystals present along the channel.

The SONICC detection in Figure 4 also illustrates the expected crystal growth trends previously mentioned and drawn out in Figure 2. The channel position closest to the gelled reservoir (P1) shows no signal most likely due to nonspontaneous nucleation (metastable) at the region of lowest protein concentration. Moving toward the protein reservoir to P2, a large number of small crystals are observed, indicating many nucleation events occurring at low ionic strength, yet at this point, the PSI trimer concentration is great enough to provide adequate starting material for crystallization to occur. Moving along further toward points P3–P6 illustrates a decrease in crystal abundance and an increase in crystal size as expected when the ionic strength increases, and more salt–protein interactions are present that reduce the number of nucleation events. We suspect the signal at the walls throughout the channel are a result of some pervaporation through PDMS causing small concentration changes at the walls when the chip was removed from the humidity chamber during the time needed for SONICC imaging. A SONICC signal was not observed at the earliest viewing of the device yet intensified as time passed. Consequently, we used the central region of the channel to determine crystal growth for further analysis.

It is also important to note that the SONICC instrument is capable of detecting nanometer-sized crystals with a spatial resolution of ~4 μm. We thus postulate the existence of nanocrystals around P2, and the upper limit crystal size range spanning to P6 is ~4 to 15 μm. Our study showed that spontaneous crystallization conditions are only present along a very small portion of the channel (~3 mm of the total channel length of 3 cm), indicating that optimal crystallization conditions are met under narrowly specific ionic strengths and protein concentrations as expected for membrane proteins such as PSI. Theoretically, this region could be spread out and shifted based on the initial protein and salt concentrations; for example, applying half the initial salt concentration used experimentally (25 mM $MgSO_4$) to the simulations would place the observed 10 day nucleation region 9.5–14.8 mm away from the gelled reservoir. However, this was not further examined due to the strict crystallization conditions adhered to by PSI; thus known, stable initial conditions were employed. Furthermore, crystals were not observed in the channel region further downstream of P6, indicating that the ionic strength was too high for spontaneous crystallization to occur as the solution has not reached the nucleation zone. As an additional confirmation of favorable crystallization conditions, a control experiment was performed where buffer containing 50 mM $MgSO_4$ was added to the gelled reservoir, maintaining a high salt concentration throughout the device. As expected, since the solution was in the nonsaturated zone, PSI crystallization was impaired and did not occur as confirmed by a lack of SONICC signal throughout the entire microchannel.

To further confirm the capabilities of this device, we also performed crystallization experiments with two other proteins, lysozyme and phycocyanin, using a different precipitant for both. Conditions were similar to the PSI experiment such that the channel was filled with precipitant and protein solution, and diffusion of precipitant out of the channel established concentration gradients. For both proteins, we observed crystallization at nucleation conditions that are in excellent agreement with previously reported conditions for these proteins. Further detail can be found in the Supporting Information.

Phase Diagram. Experimental and simulation data can be combined to develop portions of a crystallization phase diagram. Experimentally, one can observe locations along the channel where crystallization

occurs for specific incubation times, and the entire nucleation zone can even be visualized based on known initial conditions, as shown in Figure 4. At each point, crystal size can also be measured if size is an important characteristic for the application at hand. For example, in femtosecond nanocrystallography, small, monodispersed nanocrystals in solution are desired. Accordingly, determining the crystallization conditions at the channel location nearest to the gelled reservoir where crystals are still detectable (P2) would be a good starting point to make the smallest crystals. On the other hand, traditional X-ray crystallography requires large crystals to avoid X-ray damage so one could study the conditions where larger crystals are detected (*e.g.*, in the P6 region).

To accomplish such a quantitative analysis, the results of the numerical simulations were correlated to those observed experimentally. The concentration profiles developed in Figure 3 provide the concentration of the salt ions and protein (in this case Mg^{2+} and SO_4^{2-} for PSI) at any point along the channel. Furthermore, while we only simulated four time points, any duration of time can be studied. The experimental result presented in Figure 4 represents a 10 day experiment which is shown as a thick solid black line in the simulated concentration profiles. From chosen points along the channel where crystals were observed, we calculated the simulation-derived concentrations of PSI, Mg^{2+}, and SO_4^{2-}. We chose six points labeled as P1–P6 in Figure 4, which were assigned to the metastable region (P1) and spanned the nucleation zone with increasing ionic strength and protein concentration (P2 to P6).

A crystallization phase diagram conventionally compares protein concentration on the *y*-axis to salt concentration on the *x*-axis and describes the four zones of the crystallization process: *supersaturated*, *nucleation*, *metastable*, and *nonsaturated*. Figure 5 illustrates these zones as various shades of gray and black with assigned ranges of salt and protein concentration. In the case of the 10 day experiment, the metastable zone was realized at the area closest to the gelled reservoir where no SONICC signal was obtained (P1). While this lack of SONICC signal could represent either the metastable or nonsaturated zone, we assigned the metastable zone to this region as the small calculated difference in salt concentration between P1 and P2 would unlikely cause a jump from the nucleation to nonsaturated zone. In a follow-up experiment, this assignment could be confirmed by screening conditions for metastable characteristics using a seeding procedure that induces crystallization in this zone. Because the chip was imaged directly as-is with no sample extraction, we did not perform such a test.

Despite this, determining the nucleation zone of a protein is usually most sought after and was demonstrated in this experiment. Positions P2–P6 fall within

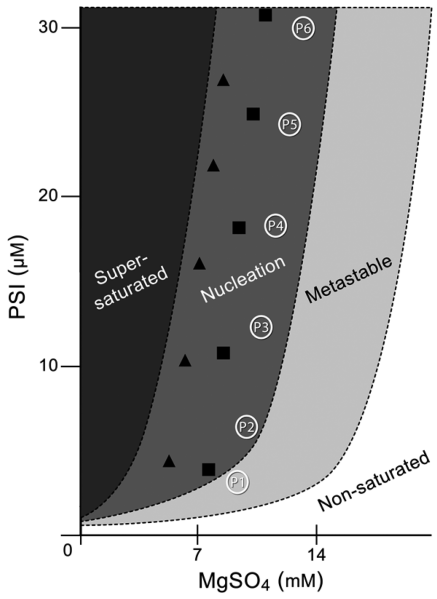

Figure 5. Possible phase diagram for PSI based on experimental and simulation data. Positions along the microchannel were correlated with simulation data to determine salt and protein concentration assignments for each phase. For the 10 day experiment, positions are labeled according to Figure 4 (P1–P6). At position P1, protein concentration was lowest and crystals were not observed, likely indicating the metastable region. P2–P6 are positions where crystals were observed, indicating conditions of the nucleation zone. Additionally, 3 (▲) and 6 (■) day experiments were performed in a similar way, and corresponding salt and protein concentrations were extracted from the simulations. For those experiments, crystals were observed at each corresponding data point indicating nucleation zone conditions. Negligible variation (~0.15 mM $MgSO_4$) was observed based on duplication of the 10 day trial; thus error bars are encompassed by the marker size.

the PSI nucleation zone where SONICC signal was observed and thus can be placed accordingly on the phase diagram in Figure 5. To our knowledge, SONICC has not been used thus far in any capillary or microfluidic crystallization procedures previously reported. This analysis methodology is extremely beneficial as the crystallization conditions tailored for small crystals such as nanocrystals can be quantified and assigned to the appropriate region of the phase diagram to aid in future crystallization trials for nanocrystallography applications. From this single experiment, a large portion of the nucleation zone was uncovered unlike in a single crystallization trial where one set of conditions (protein and salt concentrations) is screened. Specifically around position P2, the smallest crystals were observed and, due to the powerful resolving power of SONICC, likely relate to nanometer-sized crystals desired for femtosecond nanocrystallography. We also performed 3 and 6 day crystallization experiments in a similar way to further develop the nucleation zone (see triangle and square symbols in Figure 5). These results showed similar trends compared to the 10 day experiment such that all three experiments span the nucleation zone on the phase diagram. When these specific

experiments utilizing PSI were combined, the nucleation zone fell within a $MgSO_4$ concentration of ~5−13 mM and PSI concentration of ~4−30 μM, which is in agreement with values of previously determined crystallization conditions for PSI where 6−9 mM $MgSO_4$ was reported.[8] It should be noted that the 10 day trial was duplicated and negligible variation was observed between trials (~0.15 mM $MgSO_4$).

We envision this microfluidic crystallization device to be applicable to a wide range of proteins and buffer solutions due to the ability to apply the sample as-is. We demonstrated this by successfully analyzing three different proteins crystallized under very different conditions: decreasing ionic strength for PSI and increasing ionic strength for lysozyme and phycocyanin using two different salts (NaCl and ammonium sulfate, respectively). Moreover, the nucleation conditions determined for all three proteins are in excellent agreement with those previously reported (see Supporting Information for details on the crystallization of lysozyme and phycocyanin). The matching of experimental and literature nucleation zones for the three proteins is also an excellent justification for the numerical model used. We also emphasize that similar diffusion models have been used which agreed with experimental crystallization events as evidenced by others.[33,53]

Lastly, as mentioned previously, an added benefit of our novel method over diffusion-based capillary crystallization methods that generally employ a gelled protein solution[32,38−40] is the incorporation of a gel without altering the protein solution. We illustrated the versatility of this device by crystallizing PSI using the unique reverse of salting-in procedure, which has not been performed within a capillary or microfluidic crystallization device utilizing diffusion until now. Additionally, simple parallelization of several microfluidic channels with various starting conditions can also be enacted to encompass a larger portion of a protein's phase diagram, leading to rapid screening of proteins with unknown crystallization conditions. This is advantageous as more conditions can be screened in fewer experiments compared to traditional approaches. Furthermore, sample consumption in such a device is minimal (on the order of nanoliters) which is favorable for a precious protein sample where starting material is scarce. Combined, the demonstrated device can be fostered into a powerful protein crystallization tool for initial method development to determine optimal crystallization conditions of a given protein.

CONCLUSION

We demonstrated a novel microfluidic protein crystallization method for the membrane protein PSI. Crystallization of this protein is unique in that salt and protein coexist in solution initially, and salt is depleted to facilitate crystallization. This previously developed reverse of salting-in crystallization method for PSI was successfully incorporated into a microfluidic device where salt and protein concentration gradients were established by diffusion. Crystallization of PSI was realized in 3, 6, and 10 day experiments as confirmed by second harmonic generation imaging *via* SONICC, in which expected crystal growth trends were also observed. At low ionic strength regions, PSI was found as abundant small crystals, and as ionic strength increased, crystal size increased and abundance decreased. Numerical simulations provided quantification of salt ions (Mg^{2+} and SO_4^{2-}) and protein (PSI) concentration along the entire channel for various experimental durations. A portion of the PSI phase diagram could be constructed from the computed concentration values at specific time points and crystal formation imaged with SONICC at designated points along the microchannel. The nucleation zone observed with this method was in the range of that previously determined for PSI. To further support our method, we also achieved similar success with lysozyme and phycocyanin.

In the future, proteins with unknown phase diagrams and crystallization conditions can be studied with this methodology due to the versatility of the procedure where protein can be applied natively without gelling. A single microchannel experiment can encompass the entire nucleation zone of a protein for a certain starting condition. Parallel experiments can be performed to increase efficiency, and once optimal conditions are determined, they can be applied to macroscale methods for high-throughput production of crystals with desired characteristics. Collectively, an entire protein crystallization phase diagram could be pieced together more efficiently using low volumes of precious sample to better understand proteins that are not well studied. This, in tandem with highly sensitive imaging, provides a unique capability to newly developing technologies for protein studies such as femtosecond nanocrystallography where nontraditional crystallization characteristics are desired.

METHODS

Materials and Chemicals. SU-8 photoresist was purchased from Microchem, USA. *N*-Dodecyl-β-maltoside (β-DDM) was from Glycon Biochemicals, Germany. 2-(*N*-Morpholino)ethanesulfonic acid (MES), magnesium sulfate ($MgSO_4$), and low gelling temperature agarose were from Sigma-Aldrich, USA. Poly(dimethylsiloxane) (Sylgard 184) was from Dow Corning, USA, and glass microscopy slides were purchased from Fisher Scientific, USA.

Device Fabrication. The microfluidic channels were fabricated using standard photolithography and soft lithography as reported previously.[54] Briefly, AutoCAD software (Autodesk, USA)

was used to design the microchannel structure that was transferred to a chrome mask (Photosciences, USA). The mask was then used to create a silicon master wafer by patterning structures with a negative photoresist *via* photolithography. A polydimethylsiloxane (PDMS) mold was cast using the master wafer as a template in which the negative relief of the structure formed the linear microchannels in the polymer. The resulting channels measured 3 cm in length with a cross-sectional width of 50 μm and depth of 35 μm. The microchannel was cut out of the mold and oxygen plasma treated to render the PDMS surface hydrophilic and with exposed silanol groups. Reservoir holes were then punched into channel ends postexposure in order to maintain a hydrophobic surface along the reservoir walls to form the valve interface. The PDMS slab was then irreversibly bonded to an oxygen plasma-treated glass microscope slide to create a sealed channel system.

PSI Purification. PSI was isolated and purified as previously described.[8] Briefly, thylakoids isolated from cell cultures of the cyanobacterium *Thermosynechococcus elongatus* were incubated in 0.6% β-DDM to solubilize PSI. PSI was further purified by anion-exchange chromatography on a Q sepharose HP column. The column was equilibrated using a buffer containing 20 mM MES, 0.02% β-DDM, and 50 mM $MgSO_4$ (pH 6.4) at 4 °C. The salt concentration was then increased to 100 mM $MgSO_4$ to elute photosystem II and PSI monomers and further increased to 150 mM $MgSO_4$ to finally elute trimeric PSI. This protein solution was diluted to 6 mM salt, then concentrated to 10 mM chlorophyll using ultrafiltration to precipitate PSI in the form of small crystals. The final solution was made by completely dissolving the PSI microcrystals in a buffer containing 50 mM $MgSO_4$ (5 mM MES, 0.02% β-DDM, pH 6.4) to a chlorophyll concentration of 20 mM. This PSI solution was used for the microfluidic crystallization experiments described next.

PSI Crystallization and Imaging. Three microliters of PSI solution was pipetted into one empty reservoir of the microfluidic device to fill the microchannel by capillary action. Agarose was dissolved in an $MgSO_4$-free buffer containing 5 mM MES and 0.02% β-DDM at pH 6.4 (buffer A) to a concentration of 1% (w/v) by heating. Five microliters of the 1% (w/v) molten agarose buffer was pipetted into the second empty reservoir and allowed to cure at 4 °C for 15 min. Ten microliters of buffer A was then pipetted onto the gelled reservoir. The chip was placed in a dark humidity chamber to avoid PSI degradation and solution evaporation and allowed to incubate at ambient temperature for crystallization to proceed. Three separate experiments were performed with 3, 6, and 10 day incubation periods. In each case, the chip was then removed from the humidity chamber, and the microchannel was imaged with bright-field microscopy and second harmonic generation microscopy *via* SONICC (SONICC instrument, Formulatrix, USA). To capture the entire microchannel, the SONICC software was programed to acquire consecutive images along the microchannel.

Numerical Simulations. COMSOL Multiphysics 4.3 software was used to quantify the concentrations of both salt ions (Mg^{2+} and SO_4^{2-}) and PSI along the microchannel. This was done by simulating diffusion of all three species within the microchannel and reservoir. The device geometry drawn in the software was an exact replicate of the microfluidic channel system used experimentally. The Transport of Diluted Species package incorporated the diffusion coefficients of both salt ions and PSI with values presented in the Theory section. The diffusion coefficients of the ions were obtained from literature measurements in water, and the PSI diffusion coefficient in solution was estimated from the Stokes–Einstein relationship for a trimer size of 10 nm.[55] The diffusion of each species was then simulated over several time periods of 3, 6, 10, and 14 days, which allowed for the transport of the particles to be calculated. The obtained numerical solution was then used to obtain concentration profiles of the salt ions and PSI spanning the entire microchannel at the previously mentioned time points.

Conflict of Interest: The authors declare no competing financial interest.

Acknowledgment. We thank Dr. Raimund Fromme for providing phycocyanin from *T. elongatus* for experiments. Financial support from the National Institute of General Medical Sciences, National Institutes of Health Grant No. R01-GM095583 is gratefully acknowledged.

Supporting Information Available: Detailed analysis of lysozyme and phycocyanin crystallization in the microfluidic device. This material is available free of charge *via* the Internet at http://pubs.acs.org.

REFERENCES AND NOTES

1. Weber, P. C. Overview of Protein Crystallization Methods. *Methods Enzymol.* **1997**, *276*, 13–22.
2. Chayen, N. E. Comparative Studies of Protein Crystallization by Vapour-Diffusion and Microbatch Techniques. *Acta Crystallogr., Sect. D: Biol. Crystallogr.* **1998**, *54*, 8–15.
3. Vekilov, P. G.; Chernov, A. A. The Physics of Protein Crystallization. In *Solid State Physics*; Spaepen, F., Ehrenreich, H., Eds; Academic Press: New York, 2003; Vol. 57, pp 1–147.
4. McPherson, A. Introduction to Protein Crystallization. *Methods* **2004**, *34*, 254–265.
5. Drenth, J. *Principles of Protein X-ray Crystallography*, 3rd ed.; Springer Science+Business Media, LLC: New York, 2007.
6. Hunter, M. S.; DePonte, D. P.; Shapiro, D. A.; Kirian, R. A.; Wang, X.; Starodub, D.; Marchesini, S.; Weierstall, U.; Doak, R. B.; Spence, J. C.; *et al.* X-ray Diffraction from Membrane Protein Nanocrystals. *Biophys. J.* **2011**, *100*, 198–206.
7. Jordan, P.; Fromme, P.; Witt, H. T.; Klukas, O.; Saenger, W.; Krauss, N. Three-Dimensional Structure of Cyanobacterial Photosystem I at 2.5 Å Resolution. *Nature* **2001**, *411*, 909–917.
8. Fromme, P.; Witt, H. T. Improved Isolation and Crystallization of Photosystem I for Structural Analysis. *Biochim. Biophys. Acta* **1998**, *1365*, 175–184.
9. Spence, J. C.; Weierstall, U.; Chapman, H. N. X-ray Lasers for Structural and Dynamic Biology. *Rep. Prog. Phys.* **2012**, *75*, 102601.
10. Chapman, H. N.; Fromme, P.; Barty, A.; White, T. A.; Kirian, R. A.; Aquila, A.; Hunter, M. S.; Schulz, J.; DePonte, D. P.; Weierstall, U.; *et al.* Femtosecond X-ray Protein Nanocrystallography. *Nature* **2011**, *470*, 73–77.
11. Hunter, M. S.; Fromme, P. Toward Structure Determination Using Membrane-Protein Nanocrystals and Microcrystals. *Methods* **2011**, *55*, 387–404.
12. Sia, S. K.; Whitesides, G. M. Microfluidic Devices Fabricated in Poly(dimethylsiloxane) for Biological Studies. *Electrophoresis* **2003**, *24*, 3563–3576.
13. Kohlheyer, D.; Eijkel, J. C.; van den Berg, A.; Schasfoort, R. B. Miniaturizing Free-Flow Electrophoresis: A Critical Review. *Electrophoresis* **2008**, *29*, 977–993.
14. Peng, Y.; Pallandre, A.; Tran, N. T.; Taverna, M. Recent Innovations in Protein Separation on Microchips by Electrophoretic Methods. *Electrophoresis* **2008**, *29*, 157–178.
15. Wu, D.; Qin, J.; Lin, B. Electrophoretic Separations on Microfluidic Chips. *J. Chromatogr., A* **2008**, *1184*, 542–559.
16. Zhang, C.; Xu, J.; Ma, W.; Zheng, W. PCR Microfluidic Devices for DNA Amplification. *Biotechnol. Adv.* **2006**, *24*, 243–284.
17. Park, S.; Zhang, Y.; Lin, S.; Wang, T. H.; Yang, S. Advances in Microfluidic PCR for Point-of-Care Infectious Disease Diagnostics. *Biotechnol. Adv.* **2011**, *29*, 830–839.
18. Zhang, Y.; Ozdemir, P. Microfluidic DNA Amplification—A Review. *Anal. Chim. Acta* **2009**, *638*, 115–125.
19. Ng, A. H.; Uddayasankar, U.; Wheeler, A. R. Immunoassays in Microfluidic Systems. *Anal. Bioanal. Chem.* **2010**, *397*, 991–1007.
20. Bange, A.; Halsall, H. B.; Heineman, W. R. Microfluidic Immunosensor Systems. *Biosens. Bioelectron.* **2005**, *20*, 2488–2503.
21. Henares, T. G.; Mizutani, F.; Hisamoto, H. Current Development in Microfluidic Immunosensing Chip. *Anal. Chim. Acta* **2008**, *611*, 17–30.
22. Liu, K. K.; Wu, R. G.; Chuang, Y. J.; Khoo, H. S.; Huang, S. H.; Tseng, F. G. Microfluidic Systems for Biosensing. *Sensors* **2010**, *10*, 6623–6661.

23. Mir, M.; Homs, A.; Samitier, J. Integrated Electrochemical DNA Biosensors for Lab-on-a-Chip Devices. *Electrophoresis* **2009**, *30*, 3386–3397.
24. Stern, E.; Vacic, A.; Rajan, N. K.; Criscione, J. M.; Park, J.; Ilic, B. R.; Mooney, D. J.; Reed, M. A.; Fahmy, T. M. Label-Free Biomarker Detection from Whole Blood. *Nat. Nanotechnol.* **2010**, *5*, 138–142.
25. Craighead, H. Future Lab-on-a-Chip Technologies for Interrogating Individual Molecules. *Nature* **2006**, *442*, 387–393.
26. El-Ali, J.; Sorger, P. K.; Jensen, K. F. Cells on Chips. *Nature* **2006**, *442*, 403–411.
27. Psaltis, D.; Quake, S. R.; Yang, C. Developing Optofluidic Technology through the Fusion of Microfluidics and Optics. *Nature* **2006**, *442*, 381–386.
28. Yager, P.; Edwards, T.; Fu, E.; Helton, K.; Nelson, K.; Tam, M. R.; Weigl, B. H. Microfluidic Diagnostic Technologies for Global Public Health. *Nature* **2006**, *442*, 412–418.
29. Otálora, F.; Gavira, J. A.; Ng, J. D.; García-Ruiz, J. M. Counter-diffusion Methods Applied to Protein Crystallization. *Prog. Biophys. Mol. Biol.* **2009**, *101*, 26–37.
30. Gavira, J. A.; de Jesus, W.; Camara-Artigas, A.; López-Garriga, J.; García-Ruiz, J. M. Capillary Crystallization and Molecular-Replacement Solution of Haemoglobin II from the Clam *Lucina pectinata*. *Acta Crystallogr., Sect. F: Struct. Biol. Cryst. Commun.* **2006**, *62*, 196–199.
31. Kutá Smatanová, I.; Gavira, J. A.; Rezácová, P.; Vácha, F.; García-Ruiz, J. M. New Techniques for Membrane Protein Crystallization Tested on Photosystem II Core Complex of *Pisum sativum*. *Photosynth. Res.* **2006**, *90*, 255–259.
32. Dhouib, K.; Khan Malek, C.; Pfleging, W.; Gauthier-Manuel, B.; Duffait, R.; Thuillier, G.; Ferrigno, R.; Jacquamet, L.; Ohana, J.; Ferrer, J. L.; *et al.* Microfluidic Chips for the Crystallization of Biomacromolecules by Counter-Diffusion and On-Chip Crystal X-ray Analysis. *Lab Chip* **2009**, *9*, 1412–1421.
33. García-Ruiz, J. M. Counterdiffusion Methods for Macromolecular Crystallization. *Methods Enzymol.* **2003**, *368*, 130–154.
34. Song, H.; Tice, J. D.; Ismagilov, R. F. A Microfluidic System for Controlling Reaction Networks in Time. *Angew. Chem., Int. Ed.* **2003**, *42*, 768–772.
35. Zheng, B.; Roach, L. S.; Ismagilov, R. F. Screening of Protein Crystallization Conditions on a Microfluidic Chip Using Nanoliter-Size Droplets. *J. Am. Chem. Soc.* **2003**, *125*, 11170–11171.
36. Schubert, W. D.; Klukas, O.; Krauss, N.; Saenger, W.; Fromme, P.; Witt, H. T. Photosystem I of *Synechococcus elongatus* at 4 Å Resolution: Comprehensive Structure Analysis. *J. Mol. Biol.* **1997**, *272*, 741–769.
37. Lima, D.; De Wit, A. Convective Instability in Protein Crystal Growth. *Phys. Rev. E: Stat., Nonlinear, Soft Matter Phys.* **2004**, *70*, 021603.
38. Biertümpfel, C.; Basquin, J.; Suck, D.; Sauter, C. Crystallization of Biological Macromolecules Using Agarose Gel. *Acta Crystallogr., Sect. D: Biol. Crystallogr.* **2002**, *58*, 1657–1659.
39. García-Ruiz, J. M.; Novella, M. L.; Moreno, R.; Gavira, J. A. Agarose as Crystallization Media for Proteins I: Transport Processes. *J. Cryst. Growth* **2001**, *232*, 165–172.
40. Gavira, J. A.; García-Ruiz, J. M. Agarose as Crystallisation Media for Proteins II: Trapping of Gel Fibres into the Crystals. *Acta Crystallogr., Sect. D: Biol. Crystallogr.* **2002**, *58*, 1653–1656.
41. García-Ruiz, J. M.; Moreno, A.; Viedma, C.; Coll, M. Crystal Quality of Lysozyme Single Crystals Grown by the Gel Acupuncture Method. *Mater. Res. Bull.* **1993**, *28*, 541–546.
42. García-Ruiz, J. M.; Morena, A. Investigations on Protein Crystal Growth by the Gel Acupuncture Method. *Acta Crystallogr., Sect. D: Biol. Crystallogr.* **1994**, *50*, 484–490.
43. Feng, Y.; Zhou, Z.; Ye, X.; Xiong, J. Passive Valves Based on Hydrophobic Microfluidics. *Sens. Actuators, A* **2003**, *108*, 138–143.
44. Suk, J. W.; Cho, J.-H. Capillary Flow Control Using Hydrophobic Patterns. *J. Micromech. Microeng.* **2007**, *17*, N11.
45. Stokes, R. J.; Evans, D. F. *Fundamentals of Interfacial Engineering*; Wiley-VCH: New York, 1997.
46. Yuan-Hui, L.; Gregory, S. Diffusion of Ions in Sea Water and in Deep-Sea Sediments. *Geochim. Cosmochim. Acta* **1974**, *38*, 703–714.
47. Boyer, P. M.; Hsu, J. T. Experimental Studies of Restricted Protein Diffusion in an Agarose Matrix. *AIChE J.* **1992**, *38*, 259–272.
48. Crank, J. *The Mathematics of Diffusion*, 2nd ed.; Oxford University Press: New York, 1979.
49. Asherie, N. Protein Crystallization and Phase Diagrams. *Methods* **2004**, *34*, 266–272.
50. Mugele, F.; Baret, J.-C. Electrowetting: From Basics to Applications. *J. Phys.: Condens. Matter* **2005**, *17*, R705–R774.
51. Kissick, D. J.; Wanapun, D.; Simpson, G. J. Second-Order Nonlinear Optical Imaging of Chiral Crystals. *Annu. Rev. Anal. Chem.* **2011**, *4*, 419–437.
52. Wampler, R. D.; Kissick, D. J.; Dehen, C. J.; Gualtieri, E. J.; Grey, J. L.; Wang, H. F.; Thompson, D. H.; Cheng, J. X.; Simpson, G. J. Selective Detection of Protein Crystals by Second Harmonic Microscopy. *J. Am. Chem. Soc.* **2008**, *130*, 14076–14077.
53. Tanaka, H.; Inaka, K.; Sugiyama, S.; Takahashi, S.; Sano, S.; Sato, M.; Yoshitomi, S. A Simplified Counter Diffusion Method Combined with a 1D Simulation Program for Optimizing Crystallization Conditions. *J. Synchrotron Radiat.* **2004**, *11*, 45–48.
54. Nakano, A.; Camacho-Alanis, F.; Chao, T.-C.; Ros, A. Tuning Direct Current Streaming Dielectrophoresis of Proteins. *Biomicrofluidics* **2012**, *6*, 034108.
55. Boekema, E. J.; Dekker, J. P.; van Heel, M. G.; Rögner, M.; Saenger, W.; Witt, I.; Witt, H. T. Evidence for a Trimeric Organization of the Photosystem I Complex from the Thermophilic Cyanobacterium *Synechococcus* sp. *FEBS Lett.* **1987**, *217*, 283–286.